### Title

Study of Residual Stresses in Compact Tension Specimens Fabricated from Weld Metal




### Journal

Corrosion, 69(10)

### ISSN

0010-9312



### Authors

Kerr, M
Hill, MR
Olson, MD



### Publication Date

2013-10-01

### DOI

10.5006/0832

Peer reviewed

# STUDY OF RESIDUAL STRESSES IN COMPACT TENSION SPECIMENS FABRICATED FROM WELD METAL

Matthew Kerr[1,2]
US Nuclear Regulatory Commission
Office of Nuclear Regulatory Research
Washington, DC

Michael R. Hill
Hill Engineering, LLC
Rancho Cordova, CA

Mitchell D. Olson
University of California, Davis
Davis, CA

## ABSTRACT

This paper describes a preliminary investigation into the residual stress levels in welded nickel alloy compact tension specimens used in stress corrosion cracking (SCC) growth rate experiments. Results from this work document the effect of specimen size and location on residual stress profiles, the methodology outlined in this paper is appropriate to determine the degree to which residual stresses affect crack growth measurements made in coupons containing welds. Slitting method residual stress measurements (Hill Engineering and UC Davis) and finite element weld simulation (US Nuclear Regulatory Commission) have been conducted in order to evaluate both the residual stress intensity factor and residual stress profiles for two compact tension coupon blanks containing welds. The two compact tension coupon blanks were provided by Argonne National Lab (ANL) and are similar to coupons used in on-going SCC studies in weld metal. The experimental data and finite element results are in reasonable agreement, showing similar trends in calculated residual stress profiles.

## INTRODUCTION

In pressurized-water reactor (PWR) coolant systems, nickel based Dissimilar Metal (DM) welds are typically used to join carbon steel components, including the reactor pressure vessel, steam generators, and the pressurizer, to stainless steel piping. Figure 1a illustrates a representative nozzle to piping connection indicating the location of the DM weld [1-4]. The DM weld is fabricated by sequentially depositing weld passes as high-temperature molten metal that cools, solidifies, and contracts, retaining stresses that approach the material's yield strength. Pressurized water reactor piping system dissimilar metal welds are susceptible to Primary Water Stress Corrosion Cracking (PWSCC) as an active degradation mechanism. PWSCC is highly influenced by the state of stress within susceptible material with tensile residual stresses in welds being an established driving force for crack growth. Several experimental programs have focused on measuring crack growth rates in weld metal [1-3, 5], noting that crack growth rates are function of the bulk chromium concentration and the plastic strain resulting from welding [4].

In addition to crack growth rate data, component integrity assessments require accurate prediction or measurement of weld residual stresses. The US Nuclear Regulatory Commission (NRC) and Electric Power Research Institute (EPRI) are working cooperatively under a memorandum of understanding to validate weld residual stress prediction in pressurized water reactor primary cooling loop components containing dissimilar metal (DM) welds [5-9]. This paper focuses on the effect of residual stresses on SCC test specimens fabricated by Argonne National Lab (ANL) from weld metal typical of nuclear reactor piping systems and similar to coupons used in on-going SCC test programs investigating weld overlays [11-13]. Hill Engineering (HE) has used the slitting method on two compact (C(T)) coupon blanks to provide measurements of both residual stress intensity factor ($K_{RS}$) and residual stress for the coupons. These experimental measured residual stress profiles are compared to results of a Finite Element (FE) weld simulation performed by the NRC staff and sensitivity studies at UC Davis.

[1] Matthew Kerr is now with the Knolls Atomic Power Laboratory and can be reach at matthew.kerr.contractor@unnpp.gov
[2] The views expressed herein are those of the authors and do not represent an official position of the U.S. NRC.

## COUPON GEOMETRY

One method of mitigating DM welds susceptible to PWSCC is to overlay additional weld metal on the outer diameter of piping systems susceptible to PWSCC. The metal deposited in the overlay is more resistant to PWSCC, providing a structural benefit to the piping system by the addition of additional more SCC resistant material and can provide a reduction in residual stresses that drive SCC in susceptible material [15, 16]. The current work characterizes residual stress levels in C(T) coupon blanks studying SCC crack growth rates across interfaces in material from a weld overlay mockup. The C(T) coupon blanks provided by ANL were cut from a weld overlay mockup with a multi-pass double V-groove weld and weld overlay. The double V-groove weld was constructed from Alloy 182 using the Shielded Metal Arc welding process (SMAW) joining two 51 millimeter Alloy 600 plates [11, 13]. The weld overlay weld deposit was constructed from Alloy 52 using the Gas Tungsten Arc welding process (GTAW). Alloy 52 exhibits greater SCC resistance when compared to Alloy 182, primarily attributable to the higher nominal chromium content of 30 weight percent for Alloy 52 versus 16 weight percent Alloy 182 and Alloy 600. The overlay mockup is shown in
Figure **1**b and the location of the blanks relative to the weld geometry is illustrated in Figure 2. The blanks shown in Figure 3, are identical to C(T) coupons used in fracture tests, but lacking the crack-starter notch. One of the blanks has a 1T nominal in-plane geometry (characteristic width W = 50.8 mm (2.0 inch), total width W' = 1.25W, total height H = 1.20W) and out-of-plane thickness B = 12.7 mm (0.5 inch). The second blank has a 0.5T nominal in-plane geometry, with all in-plane dimensions nearly half those of the 1T coupon, and B = 12.7 mm. Actual coupon geometry differed somewhat from nominal dimensions, and is provided in Table 1.

## EXPERIMENTAL METHODS

Slitting method mechanical relaxation measurements were performed on the C(T) coupon blanks to determine residual stress. Slitting uses cutting to release residual stress and measurements of cut-induced deformation to estimate the residual stress intensity factor at a series of cut depths and the residual stress that existed prior to cutting. This is in contrast residual plastic strain measurements of welds using electron backscatter diffraction (EBSD), where variation in crystal orientation measured with EBSD is used to estimate plastic strain levels in a given weld [4, 17, 18]. These techniques are complementary in the sense that when used together they provide a more complete description of the deformation history, both elastic and plastic, of a specimen or component containing a weld.

In the current work each blank was instrumented with a strain gage as a first step, and then each blank was carefully cut along its fracture plane (i.e., along the x-axis of Figure 3). Cut depth was increased incrementally, with a strain gage reading taken after each increment of cut depth. Strain versus cut-depth data were then used to compute two results for each coupon: 1) $K_{RS}$ as a function of cut depth and 2) thickness-average residual stress as a function of position across the sample. The strain gage attached to each blank was located at the back face, centered on the thickness and on the fracture plane (i.e., at x = W' and centered on y = 0, relative to the coordinates in Figure 3). The gage was oriented to measure strain perpendicular to the fracture plane ($\varepsilon_{yy}$) and had a gage length of 3.18 mm (0.125 inch). Prior to gaging, the blank surface was prepared according to standard strain gage preparation procedures, and following gage attachment the gage area was covered with a waterproof coating. The strain measurements were taken using a commercial Wheatstone bridge designed for strain gage applications. Gages were self-temperature compensated for stainless steel and read in a quarter bridge configuration.

A wire electric discharge machine (wire EDM) was used for incremental cutting. The wire electrode diameter was 0.10 mm (0.004 inch) for the 0.5T blank and 0.25 mm (0.010 inch) for the 1T blank. For the 0.5T blank, most cut-depth increments were 0.635 mm (0.025 inch), but near the weld overlay interface, cut-depth increments were refined to 0.254 mm (0.01 inch). For the 1T blank, most cut-depth increments were 1.27 mm (0.05 inch), with increments reduced to 0.508 mm (0.02 inch) near the weld overlay interface.

Strain versus cut-depth data were used to compute $K_{RS}$ using the approach described by Schindler for a rectangular plate [14]. $K_{RS}(a)$ was computed from the influence function Z(a) provided in [14], the plane stress modulus of elasticity $E' = E$ (for Alloy 182, as given in Table 1), and the derivative of strain with respect to slit depth.

$$K_{RS}(a) = \frac{E'}{Z(a)}\frac{de}{da}$$

Where Z(a) is defined as a/W ≤ 1 – 0.616 and H/W = 0.96 for C(T) specimens:

$$Z(a) = \frac{-2.532}{(W-a)^{1/2}}\sqrt{1-\frac{\left({}^{a}/_{W} - 1 + 0.4\,{}^{H}/_{W}\right)^2}{\left(1-0.4\,{}^{H}/_{W}\right)^2}}\left[1+\left(-3.268+4.597\,{}^{H}/_{W}\right)\left(1-0.4\,{}^{H}/_{W}-{}^{a}/_{W}\right)^2 - \left(-0.028+0.316\,{}^{H}/_{W}\right)\left(1-0.4\,{}^{H}/_{W}-{}^{a}/_{W}\right)\right]$$

and for 0.616 < a/W < 1 as:

$$Z(a) = \frac{-2.532}{(W-a)^{1/2}}$$

The influence function Z(a) of [14] does not account for the holes present in the C(T) blanks, which were assumed to be of negligible effect, especially for crack sizes typical of ASTM test methods (0.2 ≤ a/W ≤ 0.9). The reference Z(a) is also applicable for a small strain gage size, which was reasonable for the 1T geometry and gage size here (gage length is 0.05W'), but was not reasonable for the 0.5T geometry (gage length is 0.1W'). An elastic correction was developed (using finite element analysis) to account for the larger strain gage size on the 0.5T blank that favorable compares to influence functions developed for C(T) specimens currently available [19]. The derivative of strain with respect to crack length was computed from the data using a moving five-point quadratic polynomial, with slope evaluated numerically at the middle point. Note that care was taken to account for the different definitions of crack size used by ASTM (measured from the hole center (i.e., the load-line)) and by Schindler (measured from the front edge).

Residual stress as a function of position across the coupon was determined from strain versus slit depth data using the approach recently described by Schajer and Prime [20] and adapted to the geometry of the C(T) coupon. The calculations require a "compliance matrix" to relate residual stress to measured strain, and this was developed from a set of elastic finite element analyses, following the approach described by Hill and Lin [21].

**FINITE ELEMENT WELD SIMULATION**

To model the residual stress distribution, the heat flow and mechanical deformation during welding were simulated using a 2D plane strain decoupled Finite Element (FE) model [1-7, 16, 22, 23] in Abaqus [10]. In a decoupled approach, first the transient heat-transfer analysis is conducted to solve the temporal and spatial distribution of the temperature in the model. This temperature distribution is then mapped to a mechanical analysis to calculate the residual stress field. Temperature dependent thermal/mechanical properties, melting, solidification, and annealing were accounted for in the analysis. A multi-pass weld simulation was performed, where a weld pass is activated when deposited and heat transfer is assumed to occur on all free surfaces of the model. The welding arc was modeled using a 2D heat source, effectively applying the heat source simultaneously over the weld bead area over the length of the weld [22]. Fabrication records and cross-sectional metallography of the weld were used to estimate weld bead geometry and pass order. The weld model used in this work is similar to those used in other thick section welds studied as part of the NRC/EPRI WRS Program [1-7] with a more detailed description of the approach below. The source material properties for the simulation were distributed as part of Phase 2 of the NRC/EPRI WRS Program [1, 7], providing uniaxial tensile test data for Alloy 182 in the annealed condition (and assumed representative of the Alloy 600, 182, and 52 sections of the weld). In order to provide an upper and lower bound estimate on weld residual stress distributions for the annealed material properties assumed in this work both isotropic and linear kinematic cases of the mechanical model are considered [23, 24]. The impact of hardening law assumptions on weld residual stress distributions and magnitudes is addressed in the discussion section of this paper.

For the Alloy 600 double V-groove weld, bead size was determined from cross-sectional metallography of the weld and fabrication history records [11, 13]. Weld beads were individually deposited in 7 groups deposited on alternating sides of the groove in order to minimize plate deflection. In total, 47 rectangular weld beads sized to match the cross-sectional metallography were modeled. The modeled weld beads are consistent in size with the 48

weld beads documented in the fabrication records, the difference in number is a result of geometric variation in weld beads in the mockup and the regular rectangular geometry modeled. After completion of the double V-groove weld, 4 backing plates were welded on to the plate bottom in order to restrain the plate during application of the overlay ( Figure **1**). A backing plate was added to the 2D model and thermal convection coefficients were scaled in order to account for the increased area of the new surfaces. Based on cross-section metallographic inspection, 170 equal sized rectangular weld beads were modeled; consistent with the 171 passes recorded in fabrication records. No temperature data was available, but current and voltage data for the weld torch were available in the fabrication information. Welding torch efficiency was adjusted to entirely melt the weld beads and match the heat affected zone in the weld cross-sections, peak torch temperature was maintained at ~3000 K for all passes. Results from related work [7, 16] indicates that estimation of heat input from cross-sectional metallography produces a reasonable estimate for residual stress profiles in thick section welds.

In the mechanical model, boundary conditions were unrestrained during welding of the double V-groove, to approximate fabrication records. During fabrication, plate deflections were minimized by balanced heat input on opposite sides of the plate (described above) and the mass of the plates (not accounted for in the model). The mechanical model for the double V-groove weld converged with no boundary conditions applied, but mesh distortions in the weld region were severe as result of excessive plate deflection in the simulation. In order to reduce plate deflection and the resulting mesh distortion in the weld model, the stiffness of the mechanical model was increased by activating all beads comprising the double V-groove weld prior to the first weld pass. Stresses developed in beads prior to welding were relieved by annealing during the weld process, as the multi-pass thermal model was used as the source for the heat input. Weld residual stress profiles calculated from the undeformed meshes in the unrestrained and 'stiffened' simulations were in agreement (stress in all principle directions were within 10%) and the 'stiffened' distortion free mesh was used in subsequent analysis in order to minimize artifacts during subsequent stress mapping of the results. The similar stress profiles calculated for the unrestrained and 'stiffened' simulations is expected as a small strain FE formulation is assumed, typical for this type of analysis, and is not sensitive to the physically unrealistic distortions calculated in the unrestrained state. To model the overlay, a backing plate was added to the model based on fabrication records and multi-pass simulation was conducted.

After completion of the weld model, stresses were mapped to a mesh with the same outer dimensions containing C(T) specimen banks at the same locations measured in the experiment. To simulate machining the C(T) specimens, excess material (including holes) was removed and to ensure stress balance, generalized plane strain elements were used. The stresses normal to the fracture plane ($\sigma_{yy}$) were extracted from C(T) blanks for comparison to the experimental data and $K_{RS}$ determination.

**RESULTS**

Strain versus cut-depth data and $K_{RS}$ computed from the slitting method are shown in Figure 4. Stress intensity factors near the weld-overlay interface are positive for both 1T and 0.5T coupon blanks, with the larger 1T geometry having higher residual stress intensity. Residual stress versus position across the coupon blank is shown in Figure 5. Values of residual stress are similar in the both geometries, except for a region of higher tensile stresses near the front face of the 1T blank. Trends in residual stress versus position from the weld-interface in the 1T and 0.5T geometries are compared in Figure 6. The figure shows comparable levels of residual stress near the interface in both geometries, with low magnitude tension to the left of the interface and low magnitude compression to the right.

Results from the FE weld model are in general agreement with the experimentally measured residual stress profiles and are plotted in Figure 7. Two simulations were performed to determine residual stress in the large block of material from which the coupon blanks were cut (shown in Figure 2), one simulation assuming isotropic hardening in the plastic material model and a second assuming linear kinematic hardening (the simulations were otherwise identical). For the 1T geometry, the kinematic result has better agreement with the experimental residual stress near the edges of the coupon (left and right sides of Figure 7(a)), but the isotropic result has somewhat better agreement away from the edges. For the 0.5T geometry, stresses are lower in magnitude and the isotropic result has better agreement with the experiment. Isotropic hardening allows for greater hardening, as the yield surface expands during both tension and compression. In the linear kinematic model, hardening is less pronounced than for the isotropic case, due to translation of the yield surface during tension and compression. In the current work, the isotropic hardening tends to over predict the stress magnitude relative to the experiment, but captures inflections in the residual stress profile that develop as a result of hardening during the welding process. A mixed or combined

hardening model, that allows both expansion and translation of the yield surface, should better capture the physics of the deformation process [23].

The residual stresses provided by the simulations were used to compute $K_{RS}$ for further comparison with the experimental results. The computation used a Green's function for the C(T) coupon recently published by Newman, et al [25] and numerical integration (paying careful attention to the singularity of the Green's function [26]). Results have mixed agreement with the experiments (Figure 8), but are similar in profile and magnitude to the experimentally generated data[3]. In the region of valid ASTM crack growth, the stress intensity factor resulting from the residual stress field ($K_{RS}$) varies as a nonlinear function of position. $K_{RS}$ varies from 0 to 8 MPa $m^{1/2}$ in the 1T blank and from -5 to 2 MPa $m^{1/2}$. in the 0.5T blank. Residual stresses in the 0.5T blank are generally lower in magnitude than for the 1T blank, primarily due to the fact that the 0.5T specimen has stress free ($\sigma_{yy}$) edges closer to the measurement plane.

**DISCUSSION**

One of the objectives of the NRC/EPRI Welding Residual Stress Programs is validating FE simulated residual stress profiles against experimental data. As part of the WRS Program an international FE round robin was conducted that includes 14 weld residual stress simulations from 9 distinct participants and comparison to experimental Deep Hole Drilling (DHD) residual stress measurements [7, 7]. Finite element analysts participating in Phase 2 of the WRS Program were supplied with a common set of material properties (the same used in the current study), as well as weld bead geometry and thermocouple data with results from this study plotted in Figure 9. In all cases there is general agreement in terms of the WRS profile shape and the DHD data along the weld centerline, visualized by the comparison of the FE averages to the DHD measurements [7]. Two averages are plotted, the average of FE results using (1) isotropic and (2) kinematic hardening as this effects the form of the WRS profile. There is better agreement between the isotropic average, in terms of profile shape and stress magnitude, though this is not the case for all locations through thickness and consistent with results presented in this paper. Further while there is general agreement between the isotropic average stresses calculated by FE and the DHD measurements, there is not consistency between the stress magnitudes calculated by the FE and the DHD measurements (i.e. the DHD results are not always high with respect to the FE results). Though the average stress from FE compared well with the experimental residual stress data, the scatter in the results can be significant for a given harden assumption ranging from ± 50 to 200 MPa depending on stress component and the location through thickness. The choice of isotropic and kinematic hardening represents an upper and lower bound for stress magnitudes for a given model, but this variation does not entirely bound the scatter in the results as a whole.

Phase 2 of the WRS program noted that (1) thermal input to the model, (2) post yield stress/strain behavior, and (3) hardening assumed had the greatest effect on the greatest impact on calculated WRS profiles [7]. In the current work, the heat input to the model is constrained by the weld macrograph and post yield stress/strain behavior is set by the material property data used, and therefore the material hardening behavior assumed will have the largest impact on the calculated residual stress profile. For an isotropic hardening material the yield surface expands when the yield stress is exceeded in either tension or compression. While in the case of a kinematic hardening material the yield surface translates on load reversal (the yield stress is lower on load reversal, capturing the Bauchinger effect). Mixed hardening captures both the expansion and translation of the yield surface on load reversal, but requires more extensive cyclic stress/strain data captured over a wide temperature range [23, 24]. All of these hardening assumptions are rate independent, therefore do not account for time dependent relaxation and the annealing implemented in the model is instantaneous (once the annealing temperature is exceeded, the plastic strain history is reset). While there is a significant amount of scatter in the application of FE WRS simulations and relatively simple material hardening assumptions are made, the Phase 2 WRS program data supports that the correct WRS profile shapes are captured and that isotropic stress profiles are in general in better agreement with experimental data.

The general agreement with the WRS profiles measured by slitting and the calculated WRS profiles assuming isotropic hardening allow sensitivity studies, regarding specimen size and extraction location, that are not feasible to conduct with physical experiments (due to the large number of samples required and expected variability) and two of such sensitivity studies are described here. The first sensitivity study consisted of translating the 0.5T blank with

[3] It should be noted that present experimental results for $K_{RS}$ and residual stress are self-consistent through the Green's function of [25]; integration of the Green's function with the residual stress in Figure 5 provides values of $K_{RS}$ very similar to those shown in Figure 4.

respect to the weld overlay and determining the stress intensity factor as a function of crack size, where the crack runs from the double V-groove weld to the weld overlay. The coupon coordinate system used for the first sensitivity study is shown in Figure 10a, where $x$ is the distance from the loading holes, $a$ is the crack length (measured from the loading holes), and $x_I$ is the distance from the loading holes to the weld interface. The second sensitivity study followed the same procedure as the first, except the 0.5T blank was rotated 180˚, so that the crack runs from the overlay toward the double V-groove weld. Consequently, the $x$ coordinate in the coupon of the second study runs along a direction opposite that in the first study (as does the crack driving direction), relative to the parent material from which the coupons are removed (compare Figure 10 a and b).

For both sensitivity studies, residual stress was determined for the 0.5T blank positioned so that the weld interface was at a specific value of $x_I/W$ and the residual stress was used to compute the residual stress intensity factor as a function of crack size. The residual stress was found by introducing residual stress from the parent block as an initial condition for a finite element mesh of the 0.5T coupon positioned at the specific value of $x_I/W$. An equilibrium residual stress field for the specific coupon location is then found by enforcing equilibrium (through the usual finite element approach) so that the coupon edges are traction free and equations of elasticity are satisfied on the interior. Residual stress on the coupon crack plane from the finite element model and the C(T) Green's function then provides the residual stress intensity factor, as described earlier. This procedure was repeated to develop residual stress and stress intensity factor for 0.5T coupons having the weld interface at $x_I/W$ = 0.20, 0.25, …, 0.90 and for the two different coupon orientations (Figure 10 a and b). Results of the sensitivity studies for the range of coupon positions (values of $x_I$) and the two coupon orientations show that position and orientation each have a significant influence on residual stress (Figure 11) and residual stress intensity factor (Figure 12). For example, a coupon with the crack running from the double V-groove weld to the overlay has a range of stress intensity factors of 0 to 2 MPa $m^{1/2}$ for a $x_I = 0.2W$ and -5 to 3 MPa $m^{1/2}$ for a $x_I = 0.9W$. The opposite is observed for a crack running from the overlay to the double V-groove weld, with a range of stress intensity factors of -5 to 3 MPa $m^{1/2}$ for a $x_I = 0.2W$ and 0 to 2 MPa $m^{1/2}$ for a $x_I = 0.9W$.

The data suggests that the levels and distribution of residual stress in the C(T) coupon blanks may have a noticeable effect on the results of fracture mechanics tests. Correction of cyclic fatigue crack propagation rates (da/dN) for the effect of residual stresses is well established with results reported in terms of the sum of applied and residual stress intensity factors [27-29]. Superposition of applied and residual stress intensity factors is generally applicable for fracture tests conducted in small-scale yielding, such as those employed to measure subcritical crack growth rates due to fatigue or SCC. The degree of the residual stress effect could be ascertained by comparing the values of $K_{RS}$ with values of stress intensity factors for applied loads. It may be useful to determine whether systematic inclusion of $K_{RS}$ could help correlate data gathered in similar materials but with coupons taken from parent plates that may have variable (unique) residual stress fields.

Insights regarding potential residual stress effects on SCC crack growth rates may be drawn by considering residual stress effects on fatigue crack growth data [27-31]. Early studies inferred the effect of residual stresses on fatigue crack growth by measuring crack tip opening displacement [30, 31], while recent work has focused on quantitative corrections for the effect of measured residual stresses on fatigue crack growth rates in fracture mechanics specimens [27-29]. Fatigue crack growth rates vary as function of residual stress level. When corrected for residual stress the fatigue crack propagation rates and near-threshold behavior for specimens containing different levels of residuals stress were found to be equivalent. Lados and Apelian note that "the effect of residual stress on crack growth rates is most pronounced at low $\Delta K$ levels (near-threshold regime), at which the applied stresses ($K_{applied}$) are low and, therefore, the ratios of residual stresses ($K_{RS}$) to applied stresses ($K_{applied}$) are high." It is difficult to comment on the effect of residual stresses on SCC propagation rates with the limited data set represented by this study, but the effect of $K_{RS}$ on SCC growth rate data is likely most affected in the same near-threshold regime as fatigue crack growth rates when $K_{applied}$ is on the order of $K_{RS}$. Lados and Apleian also note that (1) residual stress effects are lower at higher $K_{applied}$, particularly as the materials fracture toughness ($K_{1C}$) is approached and (2) below a critical $K_{RS}$ the effect of residual stresses can be ignored. Regarding point (1), SCC crack growth tests are typically well below $K_{1C}$. Regarding point (2), a larger data set correlated with experimental data is required to establish what the critical $K_{RS}$ is for SCC experiments.

**CONCLUSIONS**

The slitting method was used to quantify the magnitude of residual stress in C(T) coupon blanks and results were consistent with FE weld residual stress simulations. This paper outlines an approach that could be used to account for the effect of residual stresses in SCC test specimens using (1) FE weld models to assess the level of $K_{RS}$ in test specimens during weld/specimen design and (2) measurement of $K_{RS}$ in test specimens fabricated from weld metal using the slitting method. The following general conclusions can be drawn from this work:

- FE weld model residual stress results are in reasonable agreement with the experimentally measured residual stress distributions using the slitting method. Comparison of FE and experimental results was conducted for stresses normal to the fracture plane ($\sigma_{yy}$) for C(T) blanks containing welds. Isotropic FE stress results better capture the inflections in a residual stress than the kinematic FE stress results.

- FE weld model and experimental measurements demonstrate the effect of specimen size on residual stresses contained in a specimen, specifically smaller specimens will tend to have lower magnitude residual stress profiles than larger specimens (0.5T vs. 1T).

- FE weld model shows the pronounced effect that extraction location can have on through-thickness residual stress profiles. Specifically the edge extracted 0.5T specimen has a $K_{RS}$ profile similar in magnitude to the 1T specimen, even though the magnitude of the residual stresses has been reduced.

- It is difficult to comment on the effect of residual stresses on SCC propagation rates with the limited data set represented by this study, but the effect of $K_{RS}$ on SCC growth rate data is likely most affected in the same near-threshold regime as fatigue crack growth rates when $K_{applied}$ is on the order of $K_{RS}$.

## ACKNOWLEDGMENTS

Slitting measurements were conducted at Hill Engineering under contract from the U.S. Nuclear Regulatory Commission, Office of Nuclear Regulatory Research. Hill Engineering supported Mitch Olson through the UC Davis Internship and Career Center. Darrell Dunn (US NRC) and Bogdan Alexandreanu (ANL) supplied the C(T) weld blanks characterized in this work, as well as many insightful discussions.

## REFERENCES

1. PL Andreson, 1991, “Fracture mechancis data and modeling of environmental cracking of nickel-base alloys in high-temperature water,” Corrosion, **47**, 917-938.

2. PL Andresen and MM Mora, 2008, “Stress corrosion cracking of stainless steels and nickel alloys in high-temperature water,” Corrosion, **64**, 15-29.

3. GM Silva, AQ Bracarense, MMAM Schvartzman, 2011, “Weld heat input and stress corrosion cracking of Alloy 182 filler in a pressurized water reactor nuclear reactor coolant environment,” Corrosion, **67**, 076001-1-076001-10.

4. GA Young, MJ Hackett, JD Tucker, TE Capobianco, 2012, “Welds for nuclear systems,” Comprehensive Nuclear Materials, **4**, 273-298.

5. B Alexandreanu, OK Chopra, WJ Shack, 2008, “Crack growth rates and metallographic examinations of Alloy 600 and Alloy 82/182 from field components and laboratory materials tested in PWR environments,” in NUREG/CR-6964.

6. LF Fredette and HJ Rathbun, 2011, “NRC/EPRI welding residual stress and validation program – phase II details and findings,” in Proceedings of ASME Pressure Vessels and Piping Conference, PVP2011-57642, Baltimore, MD.

7. LF Fredette, M Kerr, HJ Rathbun, J Broussard, 2011, “NRC/EPRI welding residual stress and validation program – phase III details and findings,” in Proceedings of ASME Pressure Vessels and Piping Conference, PVP2011-57645, Baltimore, MD.

8. M Kerr and HJ Rathbun, “Summary of Finite Element (FE) sensitivity studies conducted in support of the NRC/EPRI Welding Residual Stress (WRS) Program,” in Proceedings of ASME Pressure Vessels and Piping Conference, PVP2012-78883, Toronto, ON.

9. Addendum to the Memorandum of Understanding (MOU) between NRC's Office of Nuclear Regulatory Research and Electric Power Research Institute, Inc. on Cooperative Nuclear Safety Research", NRC ADAMS Accession Number ML103490002.

10. Abaqus/Standard, version 6.10, Simulia, Inc., Providence, RI, USA, 2010.

11. B Alexandreanu, OK Chopra, WJ Shack, 2008, "Crack growth rates and metallographic examinations of Alloy 600 and Alloy 82/182 from field components and laboratory materials tested in PWR environments," in NUREG/CR-6964.

12. B Alexandreanu, 2011, "Cyclic and SCC behavior of Alloy 152 weld in a PWR environment," in Proceedings of ASME Pressure Vessels and Piping Conference, PVP2011-57463, Baltimore, MD.

13. B Alexandreanu, 2011, "SCC behavior of Alloy 52M/182 weld overlay in a PWR environment," in Proceedings of ASME Pressure Vessels and Piping Conference, PVP2011-57465, Baltimore, MD.

14. HJ Schindler, and P Bertschinger, 1997, "Some steps towards automation of the crack compliance method to measure residual stress distributions," in Proceedings of the 5th International Conference on Residual Stress, Linköping.

15. LF Fredette, PM Scott, FW Brust, A Csontos, 2009, "An analytical evaluation of the full structural weld overlay as a stress improving mitigation strategy to prevent primary water stress corrosion cracking in pressurized water reactor piping," in Proceedings of ASME Pressure Vessels and Piping Conference, PVP2009-77327, Prague, Czech Republic.

16. T Zhang, FW Brust, G Wilkowski, 2012, "Weld residual stress in various large diameter nuclear nozzles," Journal of Pressure Vessel Technology, **134**, *in press*.

17. M Kamaya, AJ Wilkinson, JM Titchmarsh, 2006, "Quantification of plastic strain of stainless steel and nickel alloy by electron backscatter diffraction," Acta Materialia, **54**, 539-548.

18. A Saez-Maderuelo, L Castro, G de Diego, 2011, "Plastic strain characterization in austenitic stainless steels and nickel alloys by electron backscatter diffraction," Journal of Nuclear Materials, **416**, 75-79.

19. MD Olson and MR Hill, 2012, "Determination of residual stress intensity factor in the compact tension coupon," Engineering Fracture Mechanics, **88**, 28-34.

20. GS Schajer and MB Prime, 2006, "Use of Inverse Solutions for Residual Stress Measurements," Journal of Engineering Materials and Technology, **128**, pp. 375-382.

21. MR Hill and W-Y Lin, 2002, "Residual stress measurement in a ceramic-metallic graded material," Journal of Engineering Materials and Technology, **124**, pp. 185-191.

22. Y Chen, D Rudland, G Wilkoski, 2004, "Impact of welding sequence of the CRDM nozzle-to-vessel weld stress analysis" in Proceedings of ASME Pressure Vessels and Piping Conference, PVP2004-2556, San Diego, CA.

23. FW Brust, T Zhang, D-J Shim, S Kalyanam, G Wilkowski, M Smith, A Goodfellow, 2010, "Summary of weld residual stress analyses for dissimilar metal weld nozzles," in Proceedings of ASME Pressure Vessels and Piping Conference, PVP2010-26106, Bellevue, WA.

24. F Dunne and Nik Petrinic, 2005, Introduction to computational plasticity, Oxford University Press.

25. JC Newman, Y Yamada, MA James, 2010, "Stress-intensity-factor equations for compact specimen subjected to concentrated forces," Engineering Fracture Mechanics, **77**, pp 1025-1029.

26. X-R Wu and AJ Carlsson, 1991, Weight function and stress intensity factor solutions, Pergamon Press, pp. 37-38.

27. DA Lados and D Apelian, 2006, "The effect of residual stress on the fatigue crack growth behavior of Al-Si_Mg cast alloys – mechanisms and corrective mathematical models," Metallurgical and Materials Transactions A, **37**, 133-145.

28. GS Wilson, AF Grandt jr, RJ Schults, 2009, "Exploiting bulk residual stresses to improve fatigue crack growth performance of structures," International Journal of Fatigue, **37**, pp. 1286-1299.

29. MR Hill and JE VanDalen, 2008, "Evaluation of residual stress corrections to fracture toughness values" Journal of ASTM International, **5**, pp. 1-11.

30. GE Nordmark, LN Mueller, RA Kelsey, 1982, "Effect of residual stresses on fatigue crack growth rates in weldments of Aluminum Ally 5456 Plate," in Residual Stress Effects in Fatigue, ASTM STP 776, American Society for Testing and Materials, pp. 44-62.

31. RC Rice, BN Leis, ME Tuttle, 1982, "An examination of the influence of residual stresses on the fatigue and fracture of railroad rail," in Residual Stress Effects in Fatigue, ASTM STP 776, American Society for Testing and Materials, pp. 132-157.

## Tables

**Table 1** Physical dimensions of C(T) blanks (in-plane dimensions defined in Figure 3, B is out-of-plane thickness)

| Dimension | Value (mm) | |
|---|---|---|
| | 1T | 0.5T |
| W | 50.8 | 24.1 |
| W' | 63.5 | 30.0 |
| H | 61.0 | 28.1 |
| D | 12.6 | 5.89 |
| B | 12.8 | 12.8 |

## Figures – grey scale figures have been individually uploaded as *.TIFF files.


**Figure 1** (a) Representative nozzle to piping weld indicating the location of the dissimilar metal weld and (b) weld overlay mockup from which C(T) coupon blanks were removed.

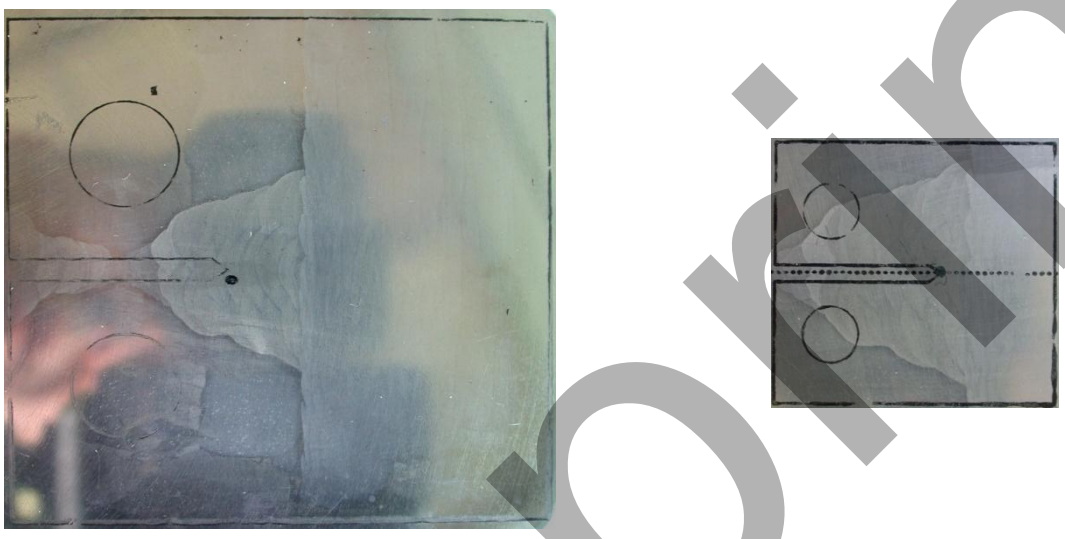

(a) (b)

**Figure 2** C(T) coupon blank locations shown on etched welded joint: (a) 1T blank and (b) 0.5T blank.

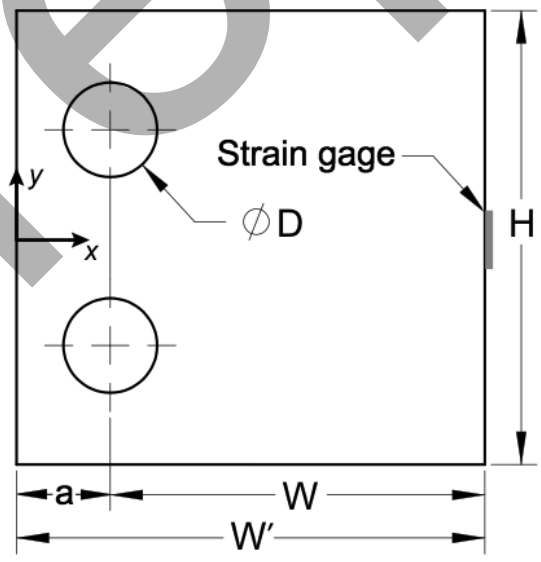


**Figure 3** C(T) coupon blank geometry and coordinate axes used in analysis; dimensions given in Table 1.

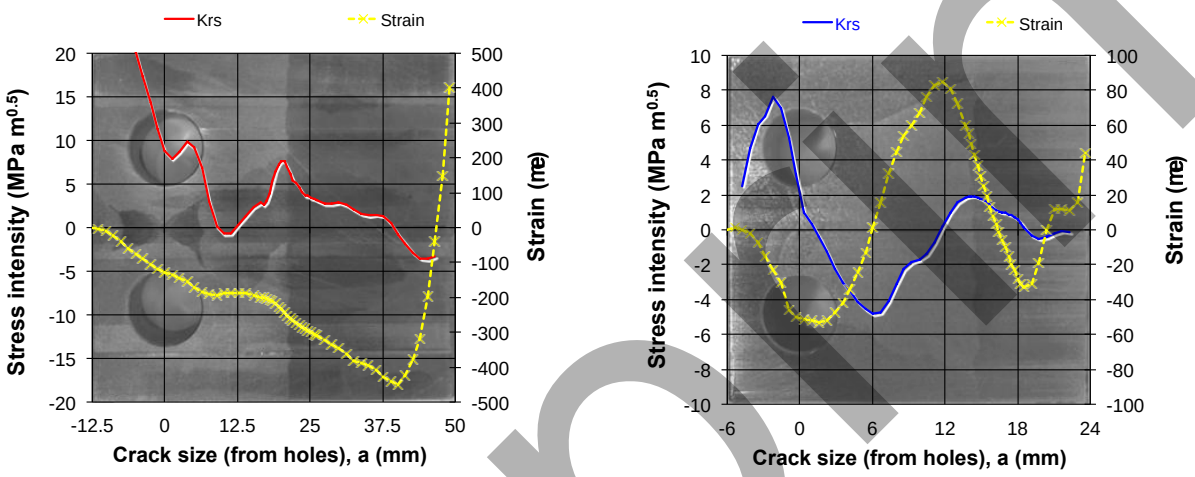


(a) (b)

**Figure 4** Residual stress intensity factors (left axis) and measured strain (right axis) for C(T) blanks: (a) 1T blank and (b) 0.5T blank. Note that με is strain x$10^{-6}$.

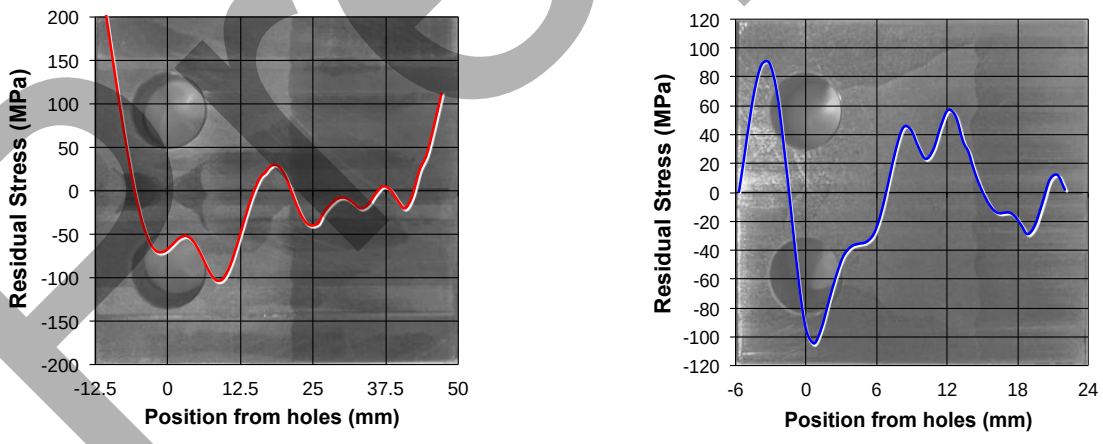


(a) (b)

**Figure 5** Residual stress computed from measured strain for C(T) blanks: (a) 1T blank and (b) 0.5T blank.

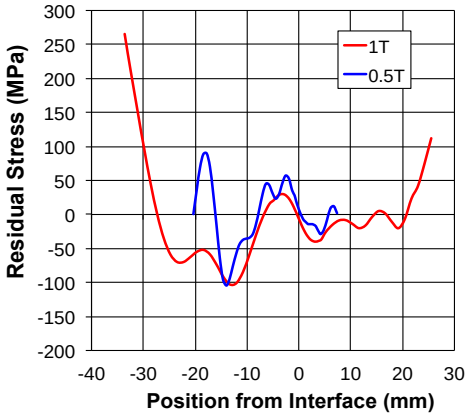


**Figure 6** Residual stress for 1T and 0.5T C(T) blanks versus position from the weld interface.

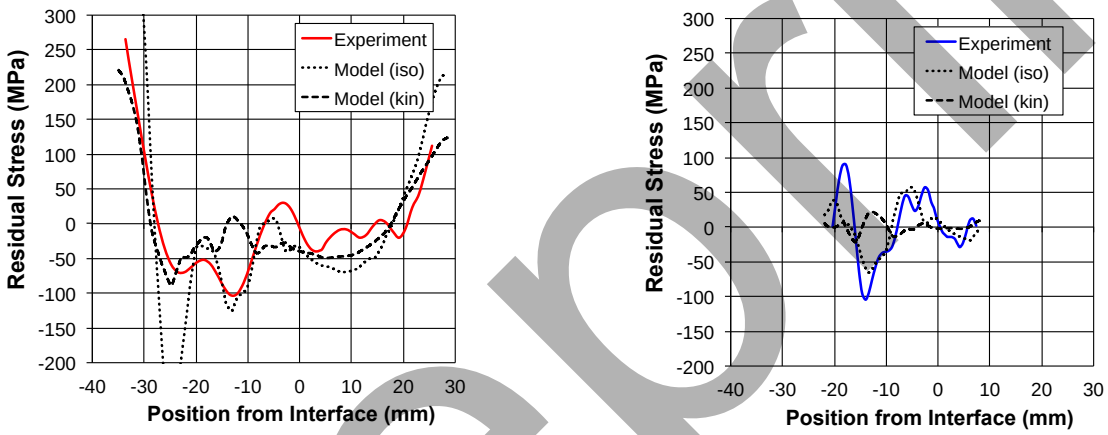


(a) (b)

**Figure 7** Comparison of residual stresses from experiment and simulation for (a) 1T and (b) 0.5T C(T) blanks; simulations assumed either isotropic (iso) or kinematic (kin) hardening.

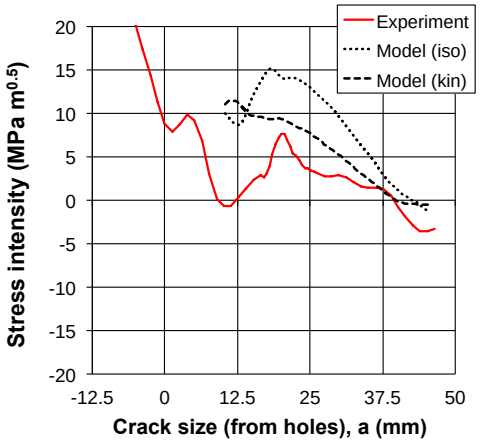


(a)

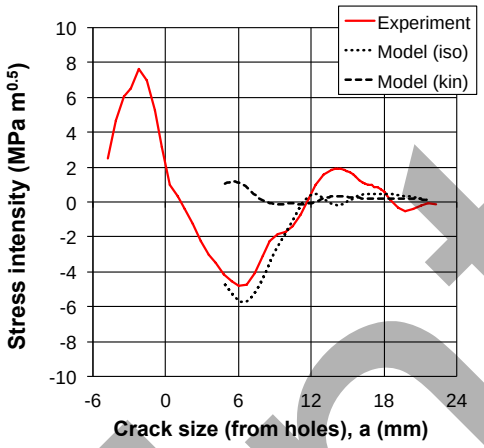


(b)

**Figure 8** Comparison of $K_{RS}$ from experiment and simulation for (a) 1T and (b) 0.5T C(T) blanks; simulations assumed either isotropic (iso) or kinematic (kin) hardening.

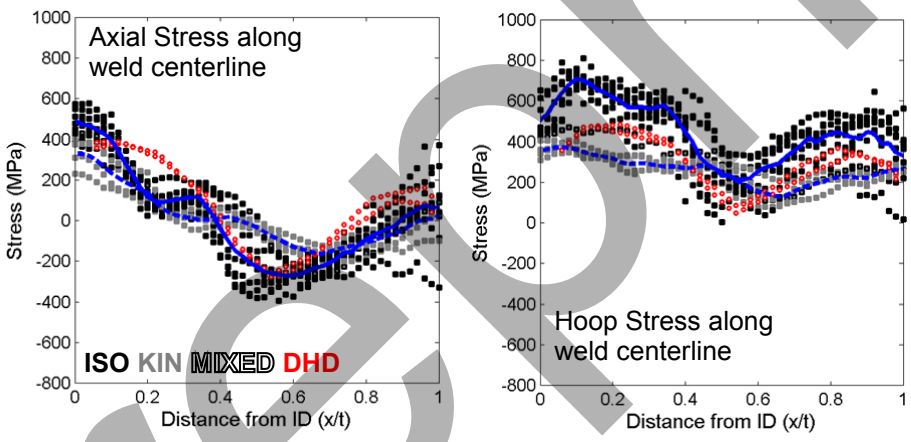


(a) (b)

**Figure 9** Results from Phase 2 of the NRC/EPRI WRS Program illustrating the effect of the of material hardening behavior on FE WRS calculations along the centerline of a thick section pipe weld, (a) axial stress component and (b) hoop stress component. Note: the dashed blue line is the average FE data using isotropic hardening and the solid blue line is the average FE data using kinematic hardening.

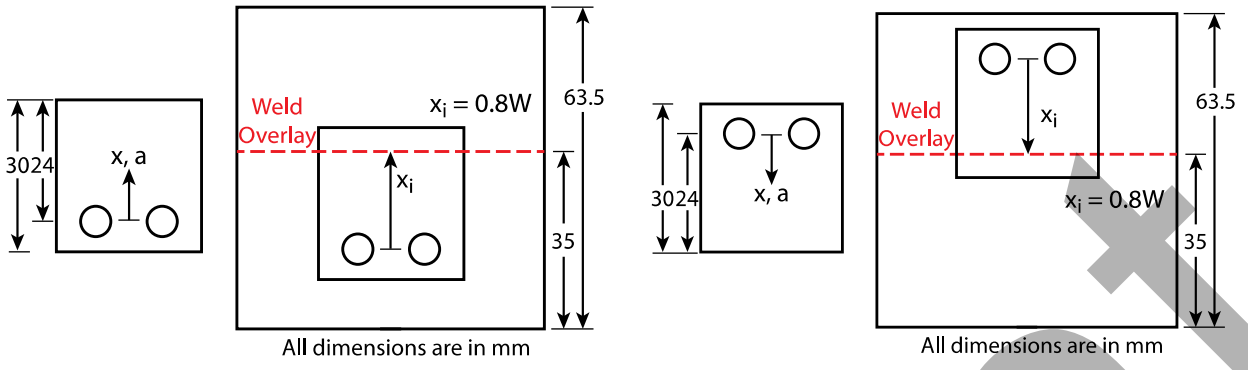


(a) (b)

**Figure 10** Coordinate systems used for the sensitivity studies, with the crack running from (a) the double V-groove weld, and (b) the overlay. Each figure shows a coupon where the weld overlay at position $x_I$ = 0.8W, where $x_I$ is measured from the holes in the coupon.

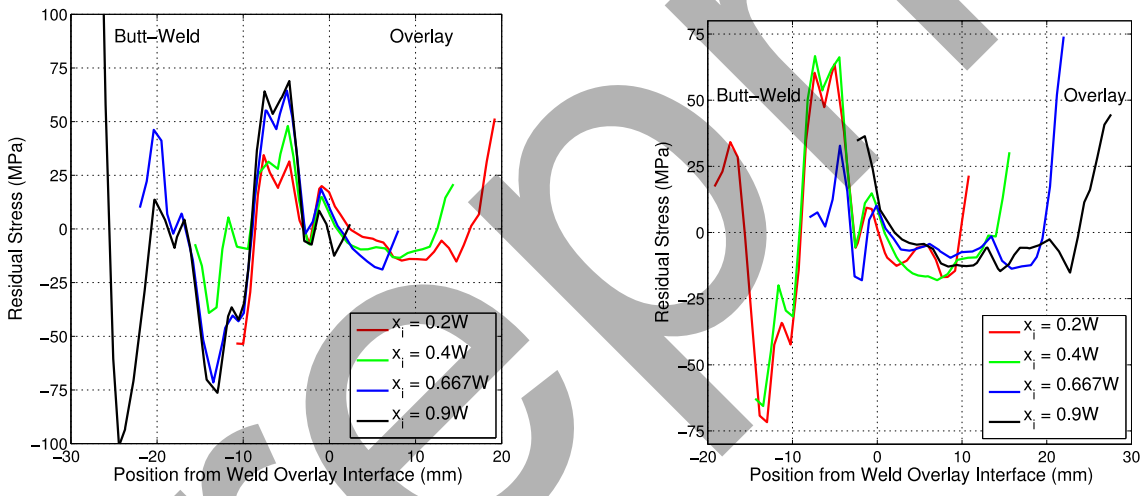


(a) (b)

**Figure 11** Residual stress at selected $x_I$ locations when the crack runs (a) from the double V-groove weld, and (b) from the overlay.

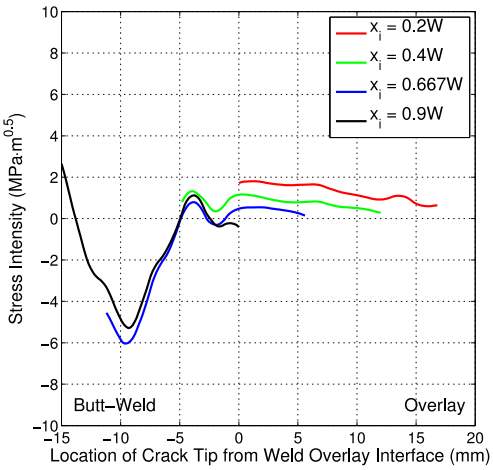


(a)

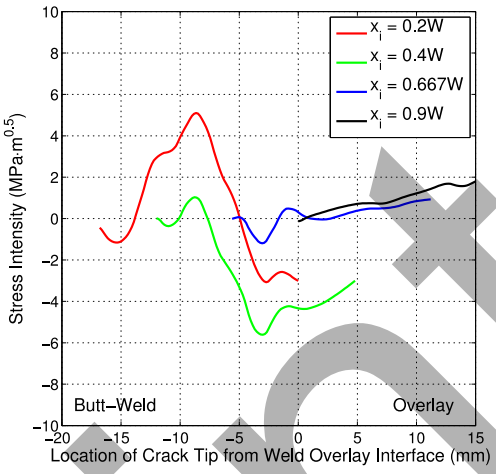


(b)

**Figure 12** Stress intensity at selected $x_I$ locations when the crack runs (a) from the double V-groove weld, and (b) from the overlay.